ACS APPLIED MATERIALS & INTERFACES

www.acsami.org

Research Article

Negative Thermal Expansion HfV_2O_7 Nanostructures for Alleviation of Thermal Stress in Nanocomposite Coatings

Guan-Wen Liu, Yuwei Zhang, Melonie P. Thomas, Ahamed Ullah, Matt Pharr,* Beth S. Guiton,* and Sarbajit Banerjee*

Cite This: *ACS Appl. Mater. Interfaces* 2021, 13, 44723−44732

Read Online

ACCESS | Metrics & More | Article Recommendations | Supporting Information

ABSTRACT: A primary mode of failure of thin-film coatings is the mismatch in thermal expansion coefficients of the substrate and the coating, which results in accumulation of interfacial stresses and ultimately in film delamination. While much attention has been devoted to modulation of interfacial bonding to mitigate delamination, current strategies are constrained in their generalizability and have had limited success in imbuing resistance to prolonged thermal cycling. We demonstrate here the incorporation of rigid thermal expansion compensators within polymeric films as a generalizable strategy for minimizing thermal mismatch with the substrate. Nanostructures of the isotropic negative thermal expansion (NTE) material HfV_2O_7 have been prepared based on the reaction of nanoparticulate precursors. The NTE behavior, derived from transverse oxygen displacement within the cubic structure, has been examined using temperature-variant powder X-ray diffraction, Raman spectroscopy, electron microscopy, and selected-area electron diffraction measurements. HfV_2O_7 initially crystallizes in a $3 \times 3 \times 3$ superlattice but undergoes phase transformations to stabilize a cubic structure that exhibits strong and isotropic NTE with a coefficient of thermal expansion (CTE) = -6.7×10^{-6} °C^{-1} across an extended temperature range of 130−700 °C. Incorporation of HfV_2O_7 in a high-temperature thermoset polybenzimidazole enables the reduction of compressive stress by 67.3% for a relatively small loading of 26.6 vol % HfV_2O_7. Based on a composite model, we demonstrate that HfV_2O_7 can reduce the thermal expansion coefficient of polymer nanocomposite films, even at low volume fractions, as a result of its substantially higher elastic modulus compared to the continuous polymer matrix. By changing the volume fraction of HfV_2O_7, the overall coefficients of thermal expansion of the film can be tuned to match a range of substrates, thereby mitigating thermal stresses and resolving a fundamental challenge for high-temperature composites and nanocomposite coatings.

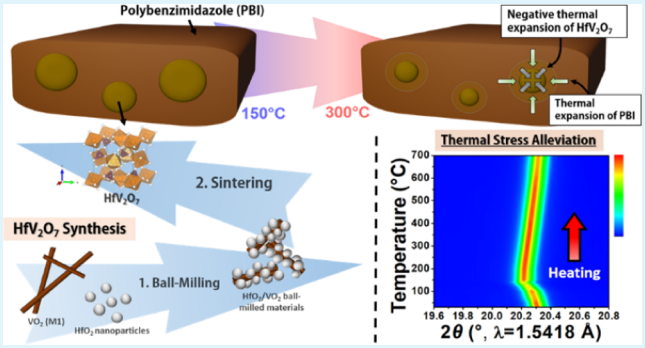

KEYWORDS: *hafnium pyrovanadate, nanostructure, negative thermal expansion, in situ TEM, thermal stress*

INTRODUCTION

Most materials expand in volume in response to thermal excitation; the specific directionality and magnitude of expansion of a solid derives from a complex interplay of phonon dispersion, lattice structure, and electronic structure.[1,2] The Grüneisen parameter, a dimensionless number, clumps together different thermodynamic quantities in a singular metric that provides a population-averaged view of thermally triggered nonlinearities in phonon dynamics.[3,4] From a practical perspective, thermal expansion is strongly implicated in materials degradation because of stresses arising from thermal gradients. Such stresses are compounded during periods of prolonged operation, giving rise to fatigue and failure.[5,6] In laminar composites and coatings, differentials in the coefficient of thermal expansion (CTE) of different materials give rise to interfacial strain and debonding upon thermal cycling.[7] As such, considerable effort has focused on the design and discovery of negative thermal expansion (NTE) materials, which are characterized by volume contraction upon heating, and thus upon incorporation within blended composites, provide a means of buffering undesirable thermal expansion.[1,2,8−10] In this work, we describe the facile synthesis of an NTE material, HfV_2O_7, from nanoparticle precursors; illustrate the NTE properties across a 570 °C temperature range using variable-temperature X-ray diffraction (XRD), Raman spectroscopy, and high-resolution transmission electron microscopy (HRTEM); and demonstrate the sharply reduced stress accumulation in polymer nanocomposite

Received: June 10, 2021
Published: September 8, 2021

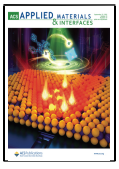

https://doi.org/10.1021/acsami.1c10867
ACS Appl. Mater. Interfaces 2021, 13, 44723−44732

coatings embedding HfV_2O_7 upon thermal cycling using multibeam optical sensor measurements.

For a specific NTE material to be of value in thermal expansion compensation, the following characteristics need to be considered: (i) the magnitude of the NTE coefficient; (ii) the directionality (isotropic or anisotropic) of NTE; and (iii) the temperature range over which NTE is manifested. The most commonly studied materials such as $Sc_2(WO_4)_3$ exhibit anisotropic NTE over a relatively narrow range of temperatures,[11−15] which limits their practical utility in thermal expansion compensators.[11,16,17] MV_2O_7 (M = Zr, Hf) compounds show quasi-isotropic NTE as a result of their cubic crystal structure. These compounds further exhibit NTE behavior across a broad temperature range and are wide-band-gap materials that have attracted considerable interest as thermally responsive components in the design of zero-thermal-expansion composites.

MV_2O_7 crystallized in the $Pa\bar{3}$ space group comprises interconnected corner-sharing MO_6 octahedra and VO_4 tetrahedra; adjacent VO_4 tetrahedra are linked by corner sharing to form a V_2O_7 unit connected by a bridging oxygen ($O_3V-O-VO_3$).[11,17−19] MV_2O_7 compounds adopt a 3 × 3 × 3 superstructure at room temperature and transform to a 1 × 1 × 1 cubic structure above about 100 °C, foreshadowing the manifestation of NTE behavior. In the low-temperature superstructure, four of the six crystallographically unique V_2O_7 groups are distorted away from 180°, whereas in the cubic structure, all of the V−O−V bridging angles are 180°.[19,20] This increasing of symmetry activates dynamic transverse vibrations of bridging oxygen atoms; these phonon modes have been directly implicated in underpinning a pronounced lattice contraction.[11] ZrV_2O_7 has a CTE of ca. -7.0×10^{-6} °C^{-1} in the range of 100−600 °C; however, an abnormal increase in NTE is observed above 600 °C as a result of a phase transition.[19] The thermal expansion of ZrV_2O_7 has been extensively tailored by substitution methods, such as single-site substitutions replacing V by P, Mo, and W,[21−24] or Zr by Hf and (Nb, Y),[18,25] as well as dual-site substitutions where Zr/V have been replaced by Fe/Mo, Fe/P, Cu/P, etc.[4,26,27] Substitution methods enable modulation of the temperature range of the NTE. For example, a phase-transition temperature as low as −48 °C is accessible with Mo substitution of ZrV_2O_7.[21] However, substitution can sometimes result in the diminution of the NTE coefficient and shrink the NTE window.[21,22,24] Furthermore, the intrinsic cubic symmetry of MV_2O_7 is broken as a result of some substitutions, such as in the case of W-substituted and Cu/P-substituted MV_2O_7.[4,22] HfV_2O_7 has been reported to have a somewhat higher CTE of ca. -7.2×10^{-6} °C^{-1} as compared to ZrV_2O_7, but has hitherto been studied only within a limited temperature range.[18] The applicability of this material in nanocomposites remains to be elucidated in the absence of viable synthesis routes to nanostructures that can be incorporated as thermal expansion compensators.[28]

Conventional solid-state synthesis routes to HfV_2O_7 require high temperatures, yield considerable impurity fractions, and as is typical of ceramic processing methods, yield micron-sized polycrystalline products that are unsuitable for incorporation within nanocomposites or coatings.[18,29−31] In this article, we demonstrate a facile solid-state synthesis route to phase-pure single-crystalline nanoparticles of HfV_2O_7 from reaction mixtures comprising HfO_2 and VO_2 nanoparticles. The NTE behavior of HfV_2O_7 has been investigated from 30 to 700 °C using temperature-dependent XRD (coupled with Rietveld refinements to derive lattice parameters), Raman spectroscopy, transmission electron microscopy, and selected-area electron diffraction (SAED). The synthesized HfV_2O_7 nanoparticles have been embedded as fillers within thin films of polybenzimidazole (PBI), a high-glass-transition-temperature engineered thermoplastic to demonstrate its application as a thermal expansion compensator. The compressive stress induced by the thermal expansion of PBI is reduced by as much as 67.3% upon thermal cycling in the 150−300 °C temperature range for 26.6 vol % loading of HfV_2O_7.

EXPERIMENTAL SECTION

HfV_2O_7 Synthesis. Hafnium pyrovanadate was prepared in nanocrystalline form based on the solid-state reaction of HfO_2 and VO_2 as per

$$2HfO_2(s) + 4VO_2(s) + O_2(g) = 2HfV_2O_7(s) \quad (1)$$

VO_2 crystallized in the M_1 monoclinic phase was purchased from Sigma-Aldrich. HfO_2 nanoparticles were synthesized using hydrothermal methods.[32] In brief, $HfCl_4$ was dissolved in 3 M NaOH aqueous solution and transferred into a poly(tetrafluoroethylene)-lined autoclave. The sealed autoclave was heated at 120 °C and maintained for 6 or 24 h to produce tetragonal or monoclinic HfO_2, respectively. The white powder products were retrieved by centrifugation and dried at 60 °C for 4 h. Bulk HfO_2 with crystallite dimensions of 120 ± 26 nm crystallized in the monoclinic phase was purchased from Sigma-Aldrich for comparison.

Stoichiometric mixtures of HfO_2 and VO_2 (total mass = 112.9 mg) were added to a 0.5 × 1 $in.^2$ polystyrene grinding vial with three 3.0 mm-sized yttria-stabilized zirconia balls and then ball-milled for 30 min at a speed of 1060 cycles/min in an 8000D Mixer/Mill. The HfO_2/VO_2 ball-milled materials were placed in a porcelain combustion boat and sintered within a tube furnace under a static air ambient at a heating rate of 60 °C/min to 600 °C. The furnace was maintained at 600 °C for 30 min. The light brown products were isolated by cooling under ambient conditions to room temperature.

PBI-HfV_2O_7 Nanocomposite Films. PBI was sourced from PBI Performance Products, Inc. (Charlotte, NC). Nanocomposite formulations were prepared by dispersing 2.3, 4.6, and 9.3 mg of HfV_2O_7 nanoparticles within 100 μL of 9 wt % PBI/dimethylacetamide (DMAc) solution using a Branson 5510R-MT ultrasonicator for 30 min. These masses correspond to 8.4, 15.3, and 26.6 vol % of HfV_2O_7 in PBI. Control samples were prepared without addition of HfV_2O_7.

Prior to coating the HfV_2O_7/PBI dispersion in DMAc, a Si wafer substrate with a thickness of 280 μm and a diameter of 50.8 mm was heated and maintained at 150 °C for 10 min on a hot plate. The ⟨100⟩ silicon wafers (resistance of 1−10 Ω/cm) were purchased from University Wafer, Inc. The dispersion was cast onto the substrate at 150 °C using a doctor blade coater. After casting, the film was cured at 150 °C for 10 min.

Structural Characterization. Powder X-ray diffraction (XRD) patterns were recorded using a Bruker D8 Advance Eco X-ray powder diffractometer equipped with a Lynxeye detector (25 kV, 40 mA) and a Cu Kα (λ = 1.5418 Å) source. In situ powder X-ray diffraction (XRD) experiments were performed using a Bruker D8-Vario X-ray powder diffractometer equipped with a Cu Kα (λ = 1.5418 Å) source operated at a 40 kV accelerating voltage with a 25 mA current. An MTC oven attachment was used for the heating experiments, which were performed under a flowing N_2 (40 sccm) environment, with patterns recorded at 50 °C intervals. Field emission transmission electron microscopy (FE-TEM) images were recorded on an FEI TECNAI G^2 F20 TEM instrument operated with an accelerating voltage of 200 kV. In situ heating Raman experiments were performed using a Jobin-Yvon HORIBA LabRAM HR800 instrument coupled to an Olympus BX41 microscope and a Linkam THMS600 temperature control stage (heating rate = 2 °C/min). Raman spectra were

https://doi.org/10.1021/acsami.1c10867
ACS Appl. Mater. Interfaces 2021, 13, 44723−44732

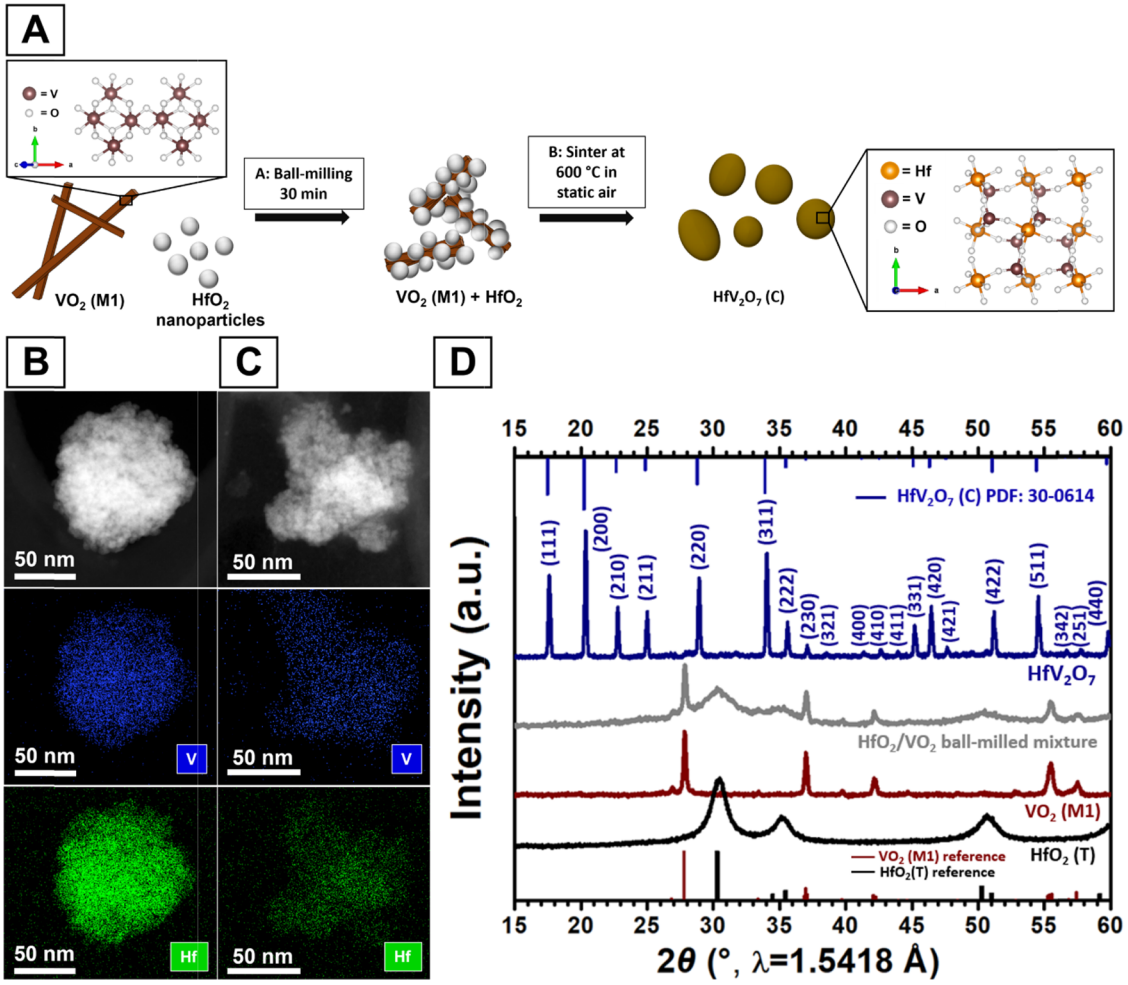

Figure 1. Direct synthesis of HfV_2O_7. (A) Schematic illustration of synthesis process. Ball-milling HfO_2 nanoparticles and VO_2 nanorods (shown in XRD pattern) at a molar ratio of 1:2 (HfO_2/VO_2) followed by annealing under static air within a tube furnace yields phase-pure HfV_2O_7 nanostructures. HAADF-STEM image and EDS elemental mapping images of (B) monoclinic HfO_2/VO_2 and (C) tetragonal HfO_2/VO_2 ball-milled mixtures. (D) Powder XRD patterns of the precursor HfO_2 nanoparticles and VO_2 nanorods, ball-milled mixture, and HfV_2O_7 product. The major reflections of HfV_2O_7 were indexed as per PDF: 30-0614.

acquired with excitation from the 514.5 nm line of an Ar-ion laser. Endothermic phase transitions were analyzed by differential scanning calorimetry (DSC, Q2000, TA Instruments) from 30 to 150 °C at a scan rate of 5 °C/min using Tzero aluminum pans under a flowing Ar atmosphere.

High-angle annular dark-field imaging (HAADF) in scanning transmission electron microscopy (STEM) mode was performed using an FEI-TALOS F200X microscope. STEM−energy-dispersive spectrometry (EDS) compositional maps and spectra generated from the maps were collected using four in-column SDD Super-X detectors in the TEM.

In Situ Heating in STEM. A small amount of the as-synthesized HfV_2O_7 powder sample was dispersed in high-purity chloroform (Sigma-Aldrich) and ultrasonicated for 30 min. Then, 10 μL of the diluted solution mixture was drop-cast onto a Protochips heating e-chip taking care to ensure that the sample did not contact multiple gold leads to short-circuit the e-chip. The drop-cast e-chips were annealed at 160 °C for 8 h in vacuum (~10^{-5} Torr) prior to the STEM characterization to burn off any contaminants on the e-chip. In situ heating TEM experiments were performed using a Nion UltraSTEM 100 (U 100) at 100 kV using the Protochips Fusion heating system.

Mechanical Characterization. The curvature of a Si substrate (ΔK) with a HfV_2O_7/PBI film coating was measured during thermal cycling using a multibeam optical stress sensor (MOS) from *k*-Space Associates. A Linkam THMS600 temperature control stage was placed on an antivibration table during thermal cycling and curvature measurements. Using Stoney's equation, the average stress change in the thin film upon thermal cycling is[33,34]

$$\Delta\sigma = \frac{E_s h_s^2}{6h_f(1-\nu_s)}\Delta K \quad (2)$$

where E_s is the elastic modulus of the silicon substrate (E_s = 195 GPa), h_s is the thickness of the substrate (h_s = 0.28 mm), ν_s is the Poisson's ratio of the substrate (ν_s = 0.2), and h_f is the thickness of thin-film electrode (measured via profilometry). The thicknesses of the HfV_2O_7/PBI films used in the experiments are 7.55 μm (0 vol % HfV_2O_7), 7.68 μm (8.4 vol % HfV_2O_7), 6.25 μm (15.3 vol % HfV_2O_7), and 8.69 μm (26.6 vol % HfV_2O_7). In this study, we take h_f as constant during each experiment such that the stress calculated is the nominal (engineering) in-plane stress. Throughout this study, the sign convention is negative for compressive stress and positive for tensile stress.

RESULTS AND DISCUSSION

Figure 1A illustrates the synthesis of HfV_2O_7 from nanoparticle precursors. In the first step, tetragonal HfO_2 nanoparticles (3.3 ± 0.7 nm; Figure 2A) prepared using hydrothermal methods have been mixed with VO_2 nanorods (374 ± 73 nm in length; Figure 2D) using ball-milling. The STEM-EDS mapping

https://doi.org/10.1021/acsami.1c10867
ACS Appl. Mater. Interfaces 2021, 13, 44723−44732

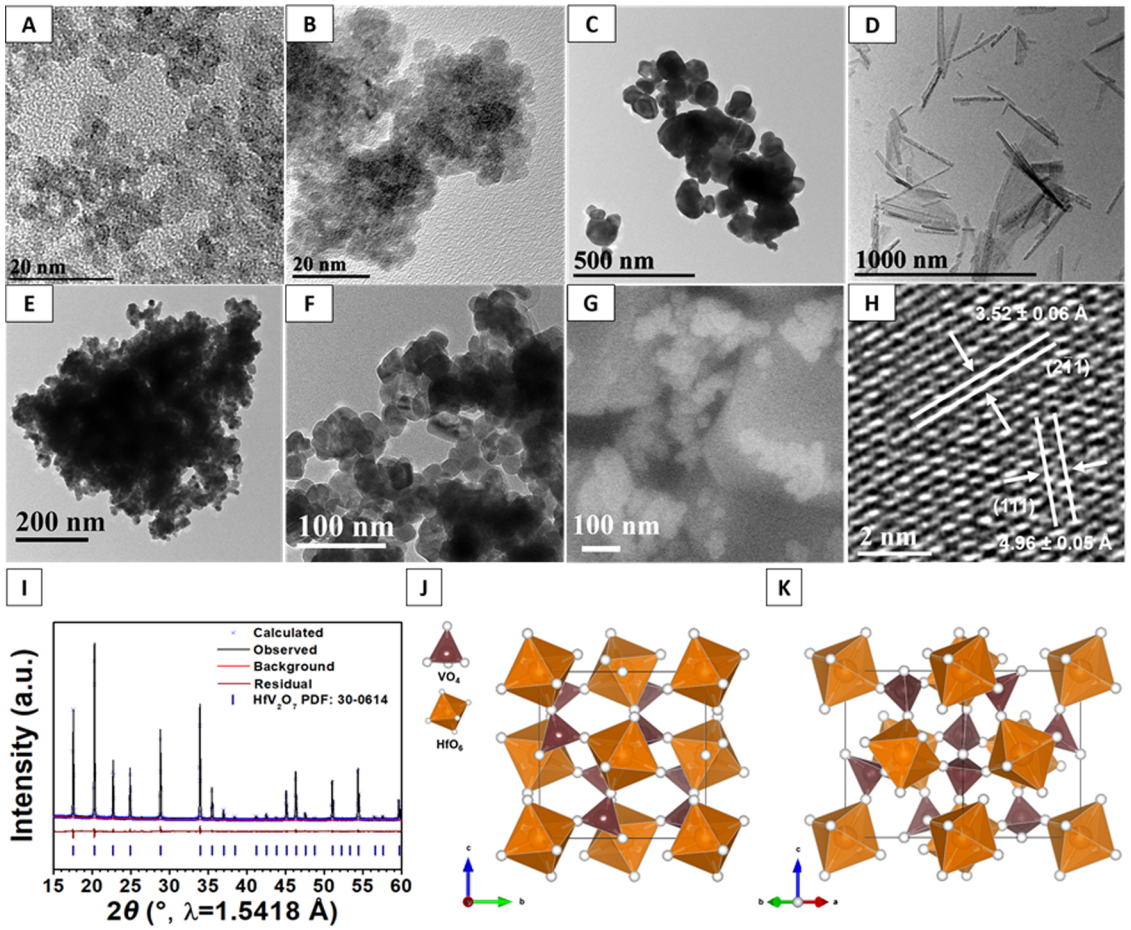

Figure 2. TEM images of (A) tetragonal HfO_2 nanoparticles, (B) monoclinic HfO_2 nanoparticles, (C) bulk monoclinic HfO_2, (D) VO_2 nanorods, and (E, F) cubic HfV_2O_7 nanoparticles. (G) SEM image of cubic HfV_2O_7 nanoparticles. (H) Lattice-resolved HRTEM image of a cubic HfV_2O_7 nanoparticle. (I) Powder X-ray diffraction pattern collected for HfV_2O_7 nanoparticles synthesized from tetragonal HfO_2 nanoparticles at 500 °C. The raw data is plotted in black; the Rietveld fit is shown as blue crosses; the background function is depicted as a red line, and the residual (observed − calculated) is depicted as a brown line. The refined HfV_2O_7 structure viewed down (J) the *a* axis and (K) 45° between the *a* and *b* axes.

images in Figure 1B,C as well as overlays of EDS maps in Figure S1 suggest that VO_2 nanorods are homogeneously covered by HfO_2 nanoparticles after ball-milling. The XRD pattern of the ball-milled mixture (Figure 1D) shows that HfO_2 nanoparticles remain in the tetragonal phase, whereas the VO_2 nanorods preserve their M_1 structure. As such, the effect of ball milling is to obtain an intimately mixed precursor powder; no chemical reactions are initiated under these conditions. In the second step, the ball-milled mixture has been sintered at 600 °C in static air to obtain cubic HfV_2O_7. Phase-pure HfV_2O_7 is obtained from stoichiometric mixtures within ca. 30 min. The XRD pattern in Figure 1D can be indexed to PDF: 30-0614 corresponding to cubic HfV_2O_7 with no discernible HfO_2 or VO_2 impurities. Miller indices are delineated in the figure for the most intense reflections. The refined HfV_2O_7 structure is shown in Figure 2I.

It is noteworthy that the nanometer-sized dimensions of the precursor materials are critical to achieving a phase-pure product at a relatively low annealing temperature. The high surface area of the nanocrystalline precursors increases the interfacial area for reactions, and the nanometer-sized dimensions ensure relatively short diffusion lengths.[35] Figure S2 shows powder X-ray diffraction patterns of HfV_2O_7 synthesized from differently sized particles and polymorphs of HfO_2.[36] When sub-micron-sized monoclinic HfO_2 (120.2 ± 25.7 nm; Figure 2C) particles are used as precursors, annealing in static air at 600 °C results in a relatively low yield of HfV_2O_7, and instead unreacted HfO_2 and oxidized V_2O_5 are observed. The conventional high-temperature synthesis of HfV_2O_7 from bulk monoclinic HfO_2 and V_2O_5 to obtain relatively high-purity HfV_2O_7 products requires more complicated processes including 3× grinding and pelletizing, 72 h annealing time, and 700 °C annealing temperature (Figure S3).[18] In contrast, tetragonal HfO_2 nanoparticles (3.3 ± 0.7 nm; Figure 2A) as well as monoclinic HfO_2 nanoparticles (5.0 ± 0.8 nm; Figure 2B) yield phase-pure HfV_2O_7 products upon reaction with VO_2 nanorods at 600 °C for only 30 min. Figure 2E−G shows the morphology of HfV_2O_7 nanostructures obtained by the reaction of tetragonal HfO_2 nanoparticles with VO_2 nanorods. The HfV_2O_7 platelets have lateral dimensions of 25.4 ± 4.4 nm. The lattice-resolved HRTEM image in Figure 2H attests to the single-crystalline nature of the particle and shows lattice separations of 4.96 ± 0.05 and 3.52 ± 0.06 Å, corresponding to the separation between (111) and (211) planes of cubic HfV_2O_7, respectively. Figure 2I shows a Rietveld refinement of the powder XRD pattern measured for HfV_2O_7 nanostructures at 500 °C (the room temperature structure is described below). Refinement

https://doi.org/10.1021/acsami.1c10867
ACS Appl. Mater. Interfaces 2021, 13, 44723−44732

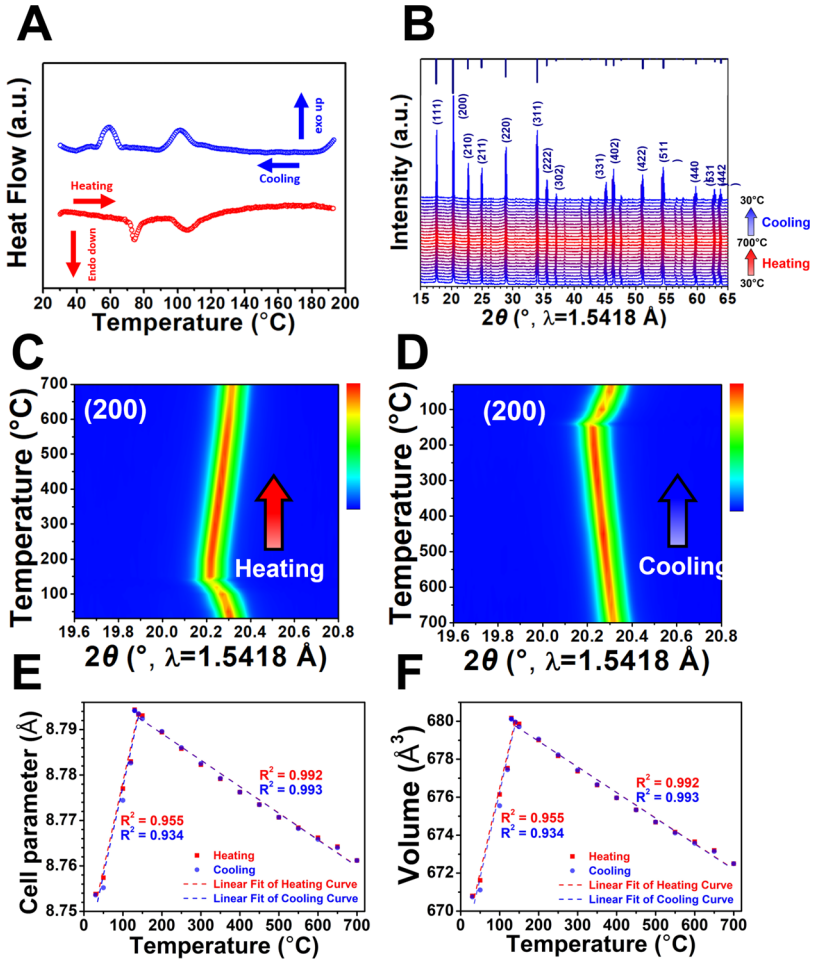

Figure 3. (A) DSC curve obtained for synthesized HfV_2O_7, indicating the phase transformations at 74 and 105 °C. (B) Temperature-dependent X-ray diffraction patterns of HfV_2O_7 (C). Patterns were collected from 30 to 700 °C at 50 °C intervals. (C, D) Heat map showing modulation plot of the (200) reflection as a function of temperature during heating and cooling. To find out the exact start point of NTE behavior, the reflections at 120, 130, and 140 °C were added in the plots. (E) Cell parameter and (F) cell volume (derived from unit cell refinements of the variable-temperature diffraction data) plotted as a function of temperature with linear fitting and R^2 values.

statistics, lattice parameters, and atom positions obtained from the Rietveld refinement are provided in Table S1. The pattern refines to cubic HfV_2O_7 in the $Pa\bar{3}$ space group with $Z = 4$ and $a = 8.77$ Å. Figure 2J,K shows two views of the crystal structure.

Figure 3A shows a DSC thermogram of HfV_2O_7 upon heating from 30 to 150 °C. Two (reversible) endothermic anomalies are associated with structural phase transitions at 74 and 105 °C. The low-temperature anomaly results from the phase transition from a 3 × 3 × 3 superstructure to an intermediate phase. The high-temperature anomaly corresponds to the transition to the high-temperature phase, which undergoes NTE. Figure S4 shows a HfV_2O_7 cubic superstructure with $a = 26.25$ Å in the $Pa\bar{3}$ space group refined from the X-ray diffraction pattern of HfV_2O_7 collected at 30 °C. The structure is refined to a $Pa\bar{3}$ structure with $a = 8.75$ Å, with a series of much weaker reflections indexed to a 3 × 3 × 3 superstructure; the structure contains 6 unique Hf sites and 11 V sites. Figure S5 reveals that this 3 × 3 × 3 superlattice exists only below 105 °C, which then transitions to the high-temperature phase that exhibits NTE behavior.

To investigate the NTE behavior of HfV_2O_7, temperature-dependent powder XRD patterns were acquired in the temperature range between 30 and 700 °C, as shown in Figure 3B–D. Consistent reflections are observed for the heating and cooling cycles, which demonstrates the high thermal stability of HfV_2O_7. In the range of 30–130 °C, the (200) reflection shifts from $2\theta = 20.31$ to 20.24°, which corresponds to an increase of the interplanar separation. However, after undergoing the transformation to the high-temperature phase and with loss of the superlattice ordering, NTE behavior is clearly manifested from 130 to 700 °C with the reflections shifted from $2\theta = 20.24$ to 20.32° (Figure 3C,D). The cell parameters of HfV_2O_7 have been refined from these patterns. Figure 3E,F plots changes in the cell parameter and cell volume of HfV_2O_7 as a function of temperature. The cell parameter decreases linearly from 8.794 to 8.761 Å with an increase in temperature from 130 to 700 °C. It is particularly notable that the NTE behavior remains linear across this entire range with $R^2 = 0.992$ for the heating cycle and $R^2 = 0.993$ for the cooling cycle, significantly surpassing the operational range for ZrV_2O_7, where a phase transition is manifested at ca. 600 °C.[19] The calculated linear thermal expansion coefficient of HfV_2O_7 is -6.7×10^{-6} °C^{-1}. The volume is decreased by 1.13% as the temperature increases from 130 to 700 °C. The overlapping cooling and heating curves demonstrate the reversibility of volume changes in HfV_2O_7.

https://doi.org/10.1021/acsami.1c10867
ACS Appl. Mater. Interfaces 2021, 13, 44723–44732

Figure 4 shows successive Raman spectra of HfV_2O_7 acquired as a function of temperature. Six bands centered at

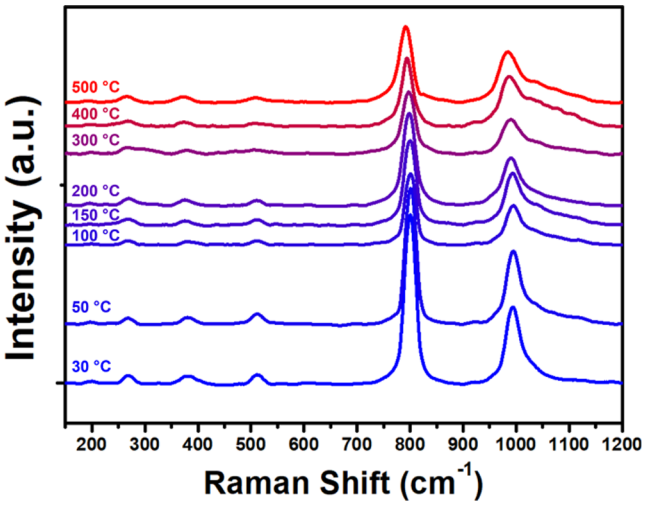

Figure 4. Raman spectroscopy of HfV_2O_7 as a function of temperature.

201, 268, 381, 512, 801, and 993 cm^{-1} are observed. The bands centered at 993 and 801 cm^{-1} are assigned to symmetric and asymmetric stretching modes of VO_4 tetrahedra, respectively.[37−39] The Raman band centered at 512 cm^{-1} is ascribed to the asymmetric bending of VO_4 tetrahedra in combination with HfO_6 octahedral stretching; the bands at 381 and 268 cm^{-1} are attributed to the symmetric bending of VO_4 tetrahedra. The low-energy vibration at 201 cm^{-1} is assigned to a lattice mode.[37−39] It is noteworthy that the characteristic Raman bands of HfV_2O_7 at 993 and 801 cm^{-1} are mostly unchanged upon heating from 30 to 150 °C, but are gradually shifted to lower frequencies with increasing temperature beyond 150 °C. Specifically, the prominent VO_4 symmetric and asymmetric stretching modes are red-shifted from 993 and 801 cm^{-1} at 150 °C to 984 and 792 cm^{-1} at 500 °C, respectively. These shifts within the NTE regime denote an elongation of V−O bond lengths, which have a pivotal role in enabling transverse vibrations to decrease the overall cell volume.

An in situ heating study performed using TEM illustrating the NTE behavior of HfV_2O_7 is shown in Figure 5. Previous work on a similar NTE material, ZrW_2O_8, indicates that upon exposure to the atmosphere, the sample absorbs moisture, forming the hydrated $ZrW_2O_7(OH)_2{\cdot}2H_2O$ phase that does now show NTE behavior.[40] To eliminate adsorbed water, the sample was heated (from 25 °C) and held at 650 °C for 5 h (in the microscope) and then cooled to 25 °C, prior to the in situ heating TEM experiments. Figure 5A,B shows the high-angle annular dark-field micrographs and their respective fast Fourier transforms (FFTs) obtained at 25 °C intervals in the temperature range of 25−250 °C. In each of these individual FFTs, two sets of spots corresponding to two sets of crystal planes of HfV_2O_7 were identified. The images in Figure 5C,D were generated by measuring distances of the red and blue spots, respectively, from the straight through beam spot. The reciprocal space distances of these spots were measured, and their real-space crystal plane *d*-spacings were computed. The temperature-dependent plots of both reciprocal space and real space distances are shown in Figure 5C,D, which indicate an increase of *d*-spacing distances up to ∼100 °C and a decrease with further increase of temperature beyond ∼100 °C, which is consistent with the in situ XRD data obtained in the same temperature range.[28,41]

Considering the strong and isotropic NTE behavior manifested in HfV_2O_7 nanoparticles, we have examined its potential as a thermal expansion compensator. PBI is a hard-glassy polymer possessing outstanding thermal and chemical stability with an upper working temperature of ca. 400 °C; it is widely used as a high-temperature protective coating for metal substrates as well as in proton exchange membranes of high-temperature fuel cells.[42,43] Given its high glass-transition temperature, it is the polymer of choice for structural applications at high temperatures. However, PBI has a thermal expansion coefficient in excess of 34×10^{-6} $°C^{-1}$ in the temperature range between 150 and 300 °C,[44−46] which can result in considerable stress accumulation at the interfaces of coated substrates, resulting inevitably in delamination upon prolonged thermal cycling.[47] In this study, HfV_2O_7 nanoparticles have been incorporated within a PBI film to reduce the large compressive stresses generated by thermal expansion.

Figures 6 and S6 show the evolution of thermal stresses that develop in a composite HfV_2O_7/PBI thin film on Si during heating with various loadings of HfV_2O_7 nanoparticles. The stress response of PBI at temperatures below 130 °C is dominated by its hygroscopicity (Figure S6). PBI has a high affinity for moisture owing to the hydrogen bonds formed between water and nitrogen and N−H groups in PBI frameworks and can absorb as much as 15 wt % of water at equilibrium.[48−50] As the temperature increases during the heating process, the evaporation of water results in the shrinkage of the PBI film, which gives rise to tensile stress in the film when constrained by the underlying substrate. At temperatures above 130 °C, the absorbed water has completely evaporated, and the observed stress behavior stems solely from the intrinsic thermal expansion behavior of PBI. Figure 6 reveals that the pristine PBI film without embedded thermal compensation fillers develops substantial compressive stress above 150 °C, ranging up to 30.7 MPa at 300 °C. The observed compressive stress is substantially mitigated with the incorporation of HfV_2O_7. The compression reduction reaches 67.3% for 26.6 vol % HfV_2O_7 incorporation with respect to the pristine PBI thin film. Still higher loadings of HfV_2O_7 nanoparticles result in a diminution of the PBI adhesion strength. The inset to Figure 6 shows three thermal stress cycles of an 8.4 vol % HfV_2O_7/PBI composite thin film from 150 to 300 °C, revealing minimal stress accumulation upon thermal cycling. Overall, the results in Figure 6 attest to the viability of the prepared HfV_2O_7 as effective thermal expansion compensators in nanocomposite thin films.

Figure S7 compares the dispersion of micron-sized HfV_2O_7, which was synthesized by conventional solid-state synthesis,[18] and HfV_2O_7 nanocrystals in the PBI matrix. The EDS elemental maps clearly demonstrate the much more homogeneous distribution of HfV_2O_7 nanocrystals compared to micron-sized particles in PBI. Distinct phase segregation is evidenced for micron-sized particles. Notably, multibeam optical stress sensor measurements probe the ensemble response across the entire film and do not probe localized stresses, e.g., those that may develop near a particle/matrix interface resulting from phase segregation.

https://doi.org/10.1021/acsami.1c10867
ACS Appl. Mater. Interfaces 2021, 13, 44723−44732

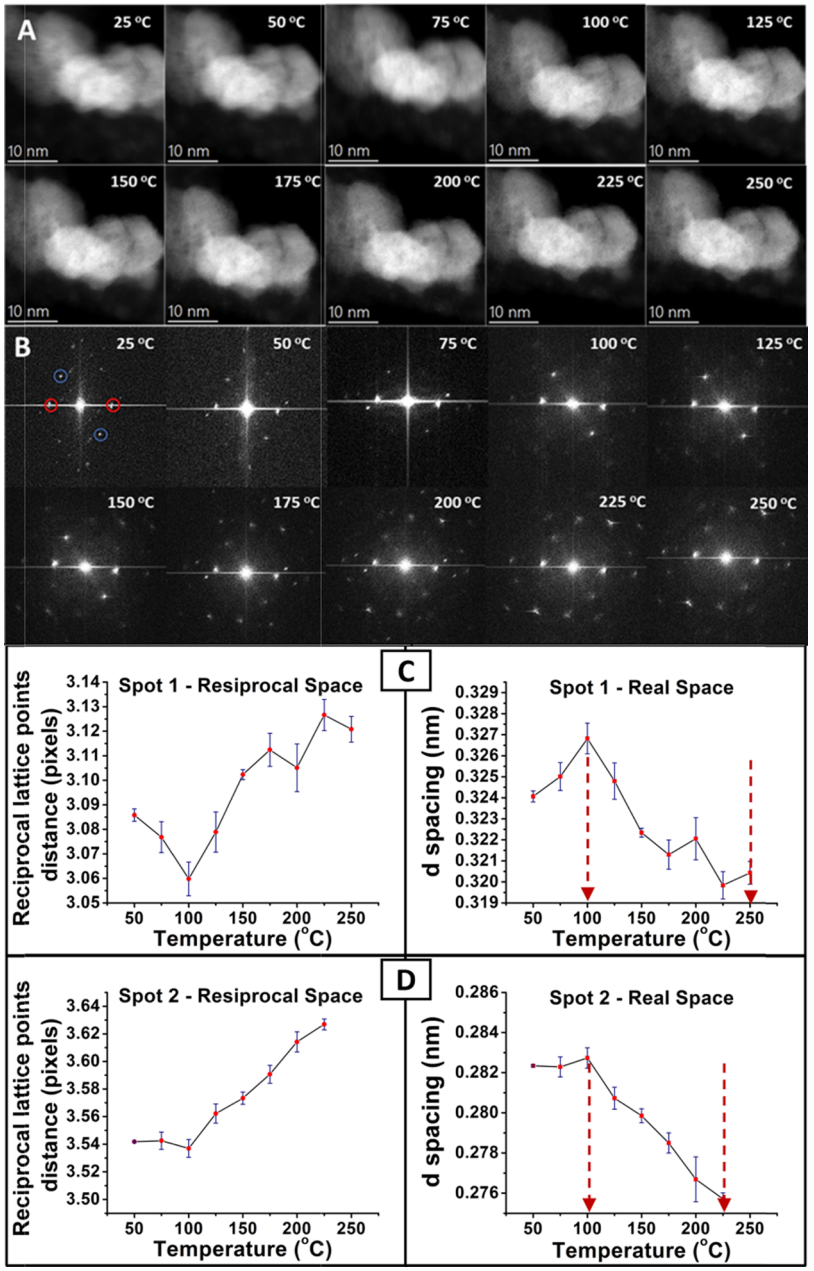

Figure 5. In situ TEM analysis of HfV_2O_7 illustrating the NTE behavior. (A, B) Individual HAADF micrographs collected every 25 °C in the temperature range of 25−250 °C and their respective FFTs. (C, D) Plots showing the temperature dependence of lattice spacing distances and their reciprocal, corresponding to spots 1 (red FFT spots) and 2 (blue FFT spots). NTE behavior is clearly evidenced between the regimes bounded by red dashed arrows.

To further elucidate the origin of the effects of incorporating HfV_2O_7 in mitigating stresses in the film, we develop a simple model. First, for the pure PBI film (without HfV_2O_7)[51]

$$\sigma_{PBI} = E_{PBI}(\alpha_{substrate} - \alpha_{PBI})\Delta T \quad (3)$$

where σ_{PBI} is the stress in the pure PBI film; E_{PBI} = 6 GPa is the elastic modulus of the PBI film;[46] $\alpha_{PBI} = 34 \times 10^{-6}$ °C^{-1} is the coefficient of thermal expansion of the pure PBI film;[44,45] $\alpha_{substrate}$ is the coefficient of thermal expansion of the Si substrate, i.e., $\alpha_{substrate} \sim 3.6 \times 10^{-6}$ °C^{-1} from 150 to 300 °C;[52] and ΔT is the temperature change, i.e., ΔT = 150 °C over the range associated with Figure 6. Substituting these values into eq 3 gives σ_{PBI} = −27.4 MPa, in which the negative sign indicates compression. This predicted value is quite similar to the measured value of −30.7 MPa for 0 vol % shown in Figure 6.

Next, to analyze the effects of incorporating HfV_2O_7 into the film, we implement commonly used models for composites[40,53,54]

$$\alpha_{composite} = \frac{f_r E_r \alpha_r + f_m E_m \alpha_m}{E_r f_r + E_m f_m} \quad (4)$$

$$E_{upper\_composite} = E_r f_r + E_m f_m,$$
$$E_{lower\_composite} = \frac{E_r E_m}{E_m f_r + E_r f_m} \quad (5)$$

https://doi.org/10.1021/acsami.1c10867
ACS Appl. Mater. Interfaces 2021, 13, 44723−44732

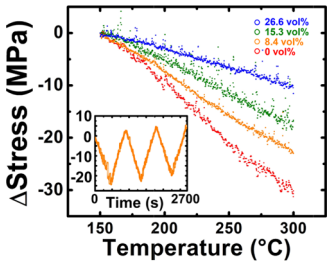

Figure 6. Evolution of thermal stresses developed in HfV_2O_7/PBI films on a Si substrate between 150 and 300 °C. The measurements are normalized taking the stress at 150 °C to be the reference point (zero stress). The inset shows three thermal stress cycles measured for an 8.4 vol % HfV_2O_7/PBI composite from 150 to 300 °C at a heating and cooling rate of 20 °C/min.

where E_r = 78 GPa and E_m = 6 GPa are the elastic moduli of HfV_2O_7 and PBI, respectively;[40,46] f_r and f_m indicate the volume fractions of HfV_2O_7 and PBI, respectively (note that $f_r + f_m = 1$); and $\alpha_r = -6.7 \times 10^{-6}$ °C^{-1} and $\alpha_m = 34 \times 10^{-6}$ °C^{-1} are the thermal expansion coefficients of HfV_2O_7 and PBI, respectively.[44,45] From eq 4 and 5, for f_r = 0.266, $\alpha_{composite} = 34.4 \times 10^{-8}$ °C^{-1}, $E_{upper\_composite}$ = 25.1 GPa, and $E_{lower\_composite}$ = 7.95 GPa.

The corresponding stress in the composite film (on the Si substrate) is[51]

$$\sigma_{composite} = E_{composite}(\alpha_{substrate} - \alpha_{composite})\Delta T \quad (6)$$

Through eq 6, the stress in the composite film equals 12.3 and 3.9 MPa by adopting upper and lower bounds on the composite modulus of eq 5 over the 150 °C temperature increase associated with Figure 6. Note that this analysis predicts small tensile stresses, which is different from the small compressive stresses observed at 26.6 vol % HfV_2O_7 in Figure 6. As such, the analysis presented in eqs 4−6 slightly overestimates the effects of incorporating HfV_2O_7 in alleviating the compressive stresses in the film. Indeed, eq 4 represents one of several existing models for the coefficient of thermal expansion of a composite; its strict validity depends on several details, e.g., shape, size, orientation, and connectivity of the reinforcement and details of bonding between the reinforcement and the matrix. Still, this simple analysis underscores the influence of the HfV_2O_7: by rapidly reducing the overall coefficient of thermal expansion, smaller compressive (more tensile) stresses are developed in the film upon the addition of HfV_2O_7. Likewise, in both the model and the measured results (Figure 6), it is evident that HfV_2O_7 can quickly reduce the thermal expansion coefficient of the composite thin film, even at relatively low volume fractions of HfV_2O_7. The source of this relatively quick reduction is evident through eq 4 by noting that the elastic modulus of HfV_2O_7 is 1 order of magnitude larger than PBI. Finally, we should note that by changing the volume fraction of HfV_2O_7, we can, in principle, tune the overall coefficients of thermal expansion of the film such that they are well matched to a range of substrates, thereby mitigating thermal stresses in various film/substrate systems.

CONCLUSIONS

In summary, we have developed a facile synthesis of phase-pure HfV_2O_7 nanoparticles starting from HfO_2 and VO_2 nanoparticles. Phase-pure products are obtained in ca. 30 min after annealing at a temperature of 600 °C. The synthesized HfV_2O_7 nanoparticles exhibit isotropic and entirely reversible NTE behavior from 130 to 700 °C with CTE = -6.7×10^{-6} °C^{-1}, as evidenced by temperature-variant powder X-ray diffraction, Raman spectroscopy, and transmission electron microscopy measurements. While Hf and Zr have similar atomic radii as a result of lanthanide contraction and their compounds show considerable homologies,[55] their phonon dispersion is substantially different. As such, HfV_2O_7 exhibits an extended linear CTE regime, whereas ZrV_2O_7 shows a sharp diminution of the CTE coefficient above 600 °C as a result of a structural phase transition.[19] The HfV_2O_7 nanoparticles have been embedded within a high-glass-transition-temperature thermoset as a thermal expansion compensator. Multibeam optical sensor measurements indicate as much as a 67.3% decrease of compressive stress upon embedding HfV_2O_7 nanoparticles within the PBI film. Based on a composite model, we demonstrate that HfV_2O_7 can rapidly reduce the thermal expansion coefficient of polymer nanocomposite films, even at low volume fractions, as a result of its substantially higher elastic modulus compared to the continuous polymer matrix. Overall, the facile synthesis strategy, manifestation of isotropic NTE across a broad temperature range, and the alleviation of compressive stress in a functional polymer nanocomposite coating at low loadings suggests a broad range of applications in high-temperature composites and nanocomposite coatings.

ASSOCIATED CONTENT

Supporting Information

The Supporting Information is available free of charge at https://pubs.acs.org/doi/10.1021/acsami.1c10867.

SEM-EDS mapping analysis on HfO_2/VO_2 ball-milled mixtures; XRD pattern of HfV_2O_7 synthesized from different HfO_2; X-ray diffraction patterns of HfV_2O_7 synthesized from conventional solid-state method; Rietveld refinement of the HfV_2O_7 structure; and XRD patterns of HfV_2O_7 collected at 30, 50, 100, 150, and 200 °C (PDF)

AUTHOR INFORMATION

Corresponding Authors

Matt Pharr − *J. Mike Walker '66 Department of Mechanical Engineering, Texas A&M University, College Station, Texas 77843-3255, United States*; Email: mpharr85@tamu.edu

Beth S. Guiton − *Department of Chemistry, University of Kentucky, Lexington, Kentucky 40506, United States*; orcid.org/0000-0002-9478-9190; Email: beth.guiton@uky.edu

Sarbajit Banerjee − *Department of Chemistry and Department of Materials Science and Engineering, Texas A&M University, College Station, Texas 77843-3255, United States*; orcid.org/0000-0002-2028-4675; Email: banerjee@chem.tamu.edu

Authors

Guan-Wen Liu − *Department of Chemistry and Department of Materials Science and Engineering, Texas A&M University, College Station, Texas 77843-3255, United States*

Yuwei Zhang − *J. Mike Walker '66 Department of Mechanical Engineering, Texas A&M University, College Station, Texas 77843-3255, United States*

https://doi.org/10.1021/acsami.1c10867
ACS Appl. Mater. Interfaces 2021, 13, 44723−44732

Melonie P. Thomas − *Department of Chemistry, University of Kentucky, Lexington, Kentucky 40506, United States*
Ahamed Ullah − *Department of Chemistry, University of Kentucky, Lexington, Kentucky 40506, United States;* orcid.org/0000-0001-9549-0003

Complete contact information is available at: https://pubs.acs.org/10.1021/acsami.1c10867

Author Contributions

G.-W.L. contributed to conceptualization, methodology, software, validation, formal analysis, investigation, writing—original draft, and visualization. Y.Z. performed formal analysis, investigation, and writing—original draft. M.P.T. conducted formal analysis, investigation, and writing—original draft. A.U. performed formal analysis. M.P. carried out supervision and writing—review and editing. B.S.G. performed supervision and writing—review and editing. S.B. conducted supervision, project administration, and writing—review and editing.

Notes

The authors declare no competing financial interest.

■ ACKNOWLEDGMENTS

The authors gratefully acknowledge support of this work from the National Science Foundation under DMR 1809866, DMR 1455154 (M.P.T. and B.S.G.), and OIA 1355438 (partial salary support for M.P.T.). Partial salary support was provided by NASA Kentucky under NASA award no.: NN15AK28A (M.P.T.). The in situ TEM data reported herein was collected at the Center for Nanophase Materials Sciences, which is a DOE Office of Science User Facility.

■ REFERENCES

(1) Sleight, A. W. Isotropic Negative Thermal Expansion. *Annu. Rev. Mater. Sci.* **1998**, *28*, 29−43.
(2) Chen, J.; Hu, L.; Deng, J.; Xing, X. Negative Thermal Expansion in Functional Materials: Controllable Thermal Expansion by Chemical Modifications. *Chem. Soc. Rev.* **2015**, *44*, 3522−3567.
(3) Erlebach, A.; Thieme, C.; Müller, C.; Hoffmann, S.; Höche, T.; Rüssel, C.; Sierka, M. Thermomechanical Properties of Zero Thermal Expansion Materials from Theory and Experiments. *Phys. Chem. Chem. Phys.* **2020**, *22*, 18518−18525.
(4) Shi, N.; Sanson, A.; Sun, Q.; Fan, L.; Venier, A.; Oliveira De Souza, D.; Xing, X.; Chen, J. Strong Negative Thermal Expansion of Cu_2PVO_7 in a Wide Temperature Range. *Chem. Mater.* **2021**, *33*, 1321−1329.
(5) Wisner, B.; Mazur, K.; Kontsos, A. The Use of Nondestructive Evaluation Methods in Fatigue: A Review. *Fatigue Fract. Eng. Mater. Struct.* **2020**, *43*, 859−878.
(6) Zhong-Yu, P.; Bin-Shi, X.; Hai-Dou, W.; Xiao-Xiao, Y. Rolling Contact Fatigue Behavior of Thermal-Sprayed Coating: A Review. *Crit. Rev. Solid State Mater. Sci.* **2020**, *45*, 429−456.
(7) Dennis, R. V.; Patil, V.; Andrews, J. L.; Aldinger, J. P.; Yadav, G. D.; Banerjee, S. Hybrid Nanostructured Coatings for Corrosion Protection of Base Metals: A Sustainability Perspective. *Mater. Res. Express* **2015**, *2*, No. 032001.
(8) Wang, L.; Yuan, P. F.; Wang, F.; Sun, Q.; Guo, Z. X.; Liang, E. J.; Jia, Y. First-Principles Investigation of Negative Thermal Expansion in II-VI Semiconductors. *Mater. Chem. Phys.* **2014**, *148*, 214−222.
(9) Mary, T. A.; Evans, J. S. O.; Vogt, T.; Sleight, A. W. Negative Thermal Expansion from 0.3 to 1050 Kelvin in ZrW_2O_8. *Science* **1996**, *272*, 90−92.
(10) Chu, C. N.; Saka, N.; Suh, N. P. Negative Thermal Expansion Ceramics: A Review. *Mater. Sci. Eng.* **1987**, *95*, 303−308.
(11) Evans, J. S. O. Negative Thermal Expansion Materials. *J. Chem. Soc., Dalton Trans.* **1999**, *19*, 3317−3326.
(12) Evans, J. S. O.; Mary, T. A.; Sleight, A. W. Negative Thermal Expansion in $Sc_2(WO_4)_3$. *J. Solid State Chem.* **1998**, *137*, 148−160.
(13) Evans, J. S. O.; Mary, T. A.; Sleight, A. W. Negative Thermal Expansion in a Large Molybdate and Tungstate Family. *J. Solid State Chem.* **1997**, *133*, 580−583.
(14) Evans, J. S. O.; Mary, T. A.; Sleight, A. W. Structure of $Zr_2(WO_4)(PO_4)_2$ from Powder X-Ray Data: Cation Ordering with No Superstructure. *J. Solid State Chem.* **1995**, *120*, 101−104.
(15) Lightfoot, P.; Woodcock, D. A.; Jorgensen, J. D.; Short, S. Low Thermal Expansion Materials: A Comparison of The Structural Behaviour of $La_{0.33}Ti_2(PO_4)_3$, $Sr_{0.5}Ti_2(PO_4)_3$ and $NaTi_2(PO_4)_3$. *Int. J. Inorg. Mater.* **1999**, *1*, 53−60.
(16) Korthuis, V.; Khosrovani, N.; Sleight, A. W.; Roberts, N.; Dupree, R.; Warren, W. W. Negative Thermal Expansion and Phase Transitions in the $ZrV_{2-x}P_xO_7$ Series. *Chem. Mater.* **1995**, *7*, 412−417.
(17) Asghar, M. H.; Placido, F.; Naseem, S. Characterization of Reactively Evaporated TiO_2 Thin Films as High and Medium Index Layers for Optical Applications. *Eur. Phys. J. Appl. Phys.* **2006**, *35*, 177−184.
(18) Hisashige, T.; Yamaguchi, T.; Tsuji, T.; Yamamura, Y. Phase Transition of $Zr_{1-x}Hf_xV_2O_7$ Solid Solutions Having Negative Thermal Expansion. *J. Ceram. Soc. Jpn.* **2006**, *114*, 607−611.
(19) Withers, R. L.; Evans, J. S. O.; Hanson, J.; Sleight, A. W. An In-Situ Temperature-Dependent Electron and X-Ray Diffraction Study of Structural Phase Transitions in ZrV_2O_7. *J. Solid State Chem.* **1998**, *137*, 161−167.
(20) Evans, J. S. O.; Hanson, J. C.; Sleight, A. W. Room-Temperature Superstructure of ZrV_2O_7. *Acta Crystallogr., Sect. B: Struct. Sci.* **1998**, *54*, 705−713.
(21) Wei, W.; Gao, Q.; Guo, J.; Chao, M.; He, L.; Chen, J.; Liang, E. Realizing Isotropic Negative Thermal Expansion Covering Room Temperature by Breaking the Superstructure of ZrV_2O_7. *Appl. Phys. Lett.* **2020**, *116*, No. 181902.
(22) Liu, Q.; Yang, J.; Sun, X.; Cheng, X.; Tang, H.; Li, H. Influence of W Doped ZrV_2O_7 on Structure, Negative Thermal Expansion Property and Photocatalytic Performance. *Appl. Surf. Sci.* **2014**, *313*, 41−47.
(23) Sahoo, P. P.; Sumithra, S.; Madras, G.; Row, T. N. G. Synthesis, Structure, Negative Thermal Expansion, and Photocatalytic Property of Mo Doped ZrV_2O_7. *Inorg. Chem.* **2011**, *50*, 8774−8781.
(24) Korthuis, V.; Khosrovani, N.; Sleight, A. W.; Roberts, N.; Dupree, R.; Warren, W. W. J. Negative Thermal Expansion and Phase Transitions in the $ZrV_{2-x}P_xO_7$ Series. *Chem. Mater.* **1995**, *7*, 412−417.
(25) Yanase, I.; Kojima, T.; Kobayashi, H. Effects of Nb and Y Substitution on Negative Thermal Expansion of $ZrV_{2-X}P_XO_7$ ($0 \leq X \leq 0.8$). *Solid State Commun.* **2011**, *151*, 595−598.
(26) Yuan, B.; Liu, X.; Song, W.; Cheng, Y.; Liang, E.; Chao, M. High Substitution of Fe^{3+} for Zr^{4+} in $ZrV_{1.6}P_{0.4}O_7$ with Small Amount of $FeV_{0.8}P_{0.2}O_4$ for Low Thermal Expansion. *Phys. Lett. A* **2014**, *378*, 3397−3401.
(27) Yuan, B.; Liu, X.; Mao, Y.; Wang, J.; Guo, J.; Cheng, Y.; Song, W.; Liang, E.; Chao, M. Low Thermal Expansion over a Wide Temperature Range of $Zr_{1-x}Fe_xV_{2-x}Mo_xO_7$ ($0 \leq x \leq 0.9$). *Mater. Chem. Phys.* **2016**, *170*, 162−167.
(28) Fleer, N. A.; Thomas, M. P.; Andrews, J. L.; Waetzig, G. R.; Gonzalez, O.; Liu, G. W.; Guiton, B. S.; Banerjee, S. Epitaxial Stabilization: Versus Interdiffusion: Synthetic Routes to Metastable Cubic HfO_2 and HfV_2O_7 from the Core-Shell Arrangement of Precursors. *Nanoscale* **2019**, *11*, 21354−21363.
(29) Korthuis, V.; Khosrovani, N.; Sleight, A. W.; Roberts, N.; Dupree, R.; Warren, W. W. Negative Thermal Expansion and Phase Transitions in the $ZrV_{2-x}P_xO_7$ Series. *Chem. Mater.* **1995**, *7*, 412−417.
(30) Turquat, C.; Muller, C.; Nigrelli, E.; Leroux, C.; Soubeyroux, J. L.; Nihoul, G. Structural Investigation of Temperature-Induced Phase Transitions in HfV_2O_7. *Eur. Phys. J. Appl. Phys.* **2000**, *10*, 15−27.
(31) Kameswari, U.; Sleight, A. W.; Evans, J. S. O. Rapid Synthesis of ZrW_2O_8 and Related Phases, and Structure Refinement of $ZrWMoO_8$. *Int. J. Inorg. Mater.* **2000**, *2*, 333−337.

(32) Wan, Y.; Zhou, X. Formation Mechanism of Hafnium Oxide Nanoparticles by a Hydrothermal Route. *RSC Adv.* **2017**, *7*, 7763−7773.
(33) Zhang, Y.; Luo, Y.; Fincher, C.; Banerjee, S.; Pharr, M. Chemo-Mechanical Degradation in V_2O_5 Thin Film Cathodes of Li-Ion Batteries during Electrochemical Cycling. *J. Mater. Chem. A* **2019**, *7*, 23922−23930.
(34) Zhang, Y.; Luo, Y.; Fincher, C.; McProuty, S.; Swenson, G.; Banerjee, S.; Pharr, M. In-Situ Measurements of Stress Evolution in Composite Sulfur Cathodes. *Energy Storage Mater.* **2019**, *16*, 491−497.
(35) Kupp, E. R.; Kochawattana, S.; Lee, S. H.; Misture, S.; Messing, G. L. Particle Size Effects on Yttrium Aluminum Garnet (YAG) Phase Formation by Solid-State Reaction. *J. Mater. Res.* **2014**, *29*, 2303−2311.
(36) Parija, A.; Waetzig, G. R.; Andrews, J. L.; Banerjee, S. Traversing Energy Landscapes Away from Equilibrium: Strategies for Accessing and Utilizing Metastable Phase Space. *J. Phys. Chem. C* **2018**, *122*, 25709−25728.
(37) Hemamala, U. L. C.; El-Ghussein, F.; Goedken, A. M.; Chen, B.; Leroux, C.; Kruger, M. B. High-Pressure X-Ray Diffraction and Raman Spectroscopy of HfV_2O_7. *Phys. Rev. B: Condens. Matter Mater. Phys.* **2004**, *70*, No. 214114.
(38) Sakuntala, T.; Arora, A. K.; Sivasubramanian, V.; Rao, R.; Kalavathi, S.; Deb, S. K. Pressure-Induced Amorphization and Decomposition in ZrV_2O_7: A Raman Spectroscopic Study. *Phys. Rev. B* **2007**, *75*, No. 174119.
(39) Hemamala, U. L. C.; El-Ghussein, F.; Muthu, D. V. S.; Krogh Andersen, A. M.; Carlson, S.; Ouyang, L.; Kruger, M. B. High-Pressure Raman and Infrared Study of ZrV_2O_7. *Solid State Commun.* **2007**, *141*, 680−684.
(40) Voigt, W. *Lehrbuch Der Krystallphysik*; B.G. Teuber: Leipzig, 1928; p 962.
(41) Yamamura, Y.; Horikoshi, A.; Yasuzuka, S.; Saitoh, H.; Saito, K. Negative Thermal Expansion Emerging upon Structural Phase Transition in ZrV_2O_7 and HfV_2O_7. *Dalton Trans.* **2011**, *40*, 2242−2248.
(42) Li, Z.-F.; Zhang, H.; Yang, F.; Stanciu, L.; Xie, J. Pt Catalysts Supported on Polybenzimidazole-Grafted Graphene for PEMFCs. *ECS Trans.* **2014**, *64*, 131−136.
(43) Aili, D.; Henkensmeier, D.; Martin, S.; Singh, B.; Hu, Y.; Jensen, J. O.; Cleemann, L. N.; Li, Q. Polybenzimidazole-Based High-Temperature Polymer Electrolyte Membrane Fuel Cells: New Insights and Recent Progress. *Electrochem. Energy Rev.* **2020**, *3*, 793−845.
(44) Chuang, S. W.; Hsu, S. L. C.; Hsu, C. L. Synthesis and Properties of Fluorine-Containing Polybenzimidazole/Montmorillonite Nanocomposite Membranes for Direct Methanol Fuel Cell Applications. *J. Power Sources* **2007**, *168*, 172−177.
(45) Shen, C. H.; Hsu, S. L.-c. Synthesis of Novel Cross-Linked Polybenzimidazole Membranes for High Temperature Proton Exchange Membrane Fuel Cells. *J. Membr. Sci.* **2013**, *443*, 138−143.
(46) Celazole PBI Material Data Sheet. https://www.gteek.com/pdf/Polybenzimidazole-PBI-rods-CelazoleI-U-60-.pdf (accessed Aug 13, 2021).
(47) Oh, K.; Chippar, P.; Ju, H. Numerical Study of Thermal Stresses in High-Temperature Proton Exchange Membrane Fuel Cell (HT-PEMFC). *Int. J. Hydrogen Energy* **2014**, *39*, 2785−2794.
(48) Brooks, N. W.; Duckett, R. A.; Rose, J.; Ward, I. M.; Clements, J. An N.M.R. Study of Absorbed Water in Polybenzimidazole. *Polymer* **1993**, *34*, 4038−4042.
(49) Zholobko, O.; Wu, X. F.; Zhou, Z.; Aulich, T.; Thakare, J.; Hurley, J. A Comparative Experimental Study of the Hygroscopic and Mechanical Behaviors of Electrospun Nanofiber Membranes and Solution-Cast Films of Polybenzimidazole. *J. Appl. Polym. Sci.* **2020**, *137*, No. 49639.
(50) Paglia, L.; Genova, V.; Bracciale, M. P.; Bartuli, C.; Marra, F.; Natali, M.; Pulci, G. Thermochemical Characterization of Polybenzimidazole with and without Nano-ZrO_2 for Ablative Materials Application. *J. Therm. Anal. Calorim.* **2020**, *142*, 2149−2161.
(51) Ashby, M. F. Criteria for Selecting the Components of Composites. *Acta Metall. Mater.* **1993**, *41*, 1313−1335.
(52) White, G. K.; Minges, M. L. Thermophysical Properties of Some Key Solids: An Update. *Int. J. Thermophys.* **1997**, *18*, 1269−1327.
(53) Levin, V. M. Thermal Expansion Coefficient of Heterogeneous Materials. *Mech. Solids* **1967**, *2*, 58−61.
(54) Reuss, A. Berechnung Der Fließgrenze von Mischkristallen Auf Grund Der Plastizitätsbedingung Für Einkristalle. *Z. Angew. Math. Mech.* **1929**, *9*, 49−58.
(55) Depner, S. W.; Cultrara, N. D.; Farley, K. E.; Qin, Y.; Banerjee, S. Ferroelastic Domain Organization and Precursor Control of Size in Solution-Grown Hafnium Dioxide Nanorods. *ACS Nano* **2014**, *8*, 4678−4688.

https://doi.org/10.1021/acsami.1c10867
ACS Appl. Mater. Interfaces 2021, 13, 44723−44732